Scientific Research Publishing

Journal of Geoscience and Environment Protection, 2024, 12, 322-342
https://www.scirp.org/journal/gep
ISSN Online: 2327-4344
ISSN Print: 2327-4336

Development and Applications of a Coupled Circulation-Ice Modelling System with Nesting Capacity for the Northwest Atlantic

Jinyu Sheng, Qiantong Pei, Yi Sui, Bo Yang, Shengmu Yang, Kyoko Ohashi

Department of Oceanography, Dalhousie University, Halifax, Canada
Email: Jinyu.Sheng@Dal.Ca

How to cite this paper: Sheng, J. Y., Pei, Q. T., Sui, Y., Yang, B., Yang, S. M., & Ohashi, K. (2024). Development and Applications of a Coupled Circulation-Ice Modelling System with Nesting Capacity for the Northwest Atlantic. *Journal of Geoscience and Environment Protection, 12,* 322-342.
https://doi.org/10.4236/gep.2024.126020

Received: May 24, 2024
Accepted: June 25, 2024
Published: June 28, 2024

Abstract

A coupled circulation-ice modelling system with multi-grid nesting capacity was developed for the northwest Atlantic (CCIMS-nwA) based on the Regional Ocean Modeling System (ROMS) and Los Alamos Sea Ice Model (CICE). CCIMS-nwA is forced by reanalysis-derived atmospheric fields at the surface, tidal forcing, inflows and ice conditions specified at lateral open boundaries, riverine freshwater discharges, and continental runoff due to melting of ice and snow over land. Different nested-grid setups were used based on requirements of different projects. Performance of CCIMS-nwA is assessed using the in-situ oceanographic observations, satellite remote sensing data, and ocean reanalysis. Model results in three applications demonstrate the feasibility and skills of CCIMs-nwA in simulating both the large-scale hydrodynamics over the eastern Canadian shelf and fine-resolution currents and hydrography over coastal waters.

Keywords

Ocean Circulation, Hydrodynamics, Sea Ice, Tides, Northwest Atlantic, Numerical Modelling, Nested-Grid, Three-Dimensional, Model Performance, Dissolved Oxygen, Residence Time, Freshwater Thickness

1. Introduction

The eastern Canadian shelf (ECS) and adjacent deep ocean waters of the northwestern Atlantic (nwA) are the regions with the most challenging marine environments in the world. Previous studies demonstrated that the ECS has large seasonal and interannual variability in temperature and salinity (Petrie & Anderson, 1983; Petrie & Drinkwater, 1993; Urrego-Blanco & Sheng, 2012). The

annual cycle of the sea surface temperature (SST) over the ECS is among the largest in the global ocean, with the maximum seasonal variation of SST observed to be ~18˚C (Thompson et al., 1988). The three-dimensional (3D) currents and hydrography over the nwA are affected by two large-scale ocean currents: the Gulf Stream and Labrador Current (**Figure 1**). The 3D hydrodynamics over the ECS are also affected by tidal forcing, with the maximum tidal ranges observed to be ~16 m in the Bay of Fundy and Ungava Bay. The northern part of the ECS (including Baffin Bay, Labrador Shelf, northern Newfoundland Shelf and Gulf of St. Lawrence) has large seasonal changes in sea ice (Yashayaev et al., 2022). Reliable knowledge of time-dependent and 3D circulation and hydrography over the ECS are needed for effective management of marine resources over the region, including fisheries, aquaculture, navigation, recreation, and offshore energy oil and gas development.

As part of a multi-disciplinary research project known as "the North Atlantic as a climate ocean", which has been funded by the Canada First Research Excellence Fund (CFREF) through the Ocean Frontier Institute (OFI) at Dalhousie University of Canada, an advanced physical-biogeochemical (BGC) modelling platform was developed for providing regional estimates of the ocean state with a focus on productivity and the biological carbon pump over the ECS. The physical component of this modelling platform is the coupled circulation-ice modelling system for the nwA with multi-grid nesting capacity (CCIMS-nwA). The main objectives of this paper are to present this advanced modelling system and to discuss model results in three applications of CCIMS-nwA. The structure of this paper is as follows. Sections 2 and 3 describe the model setup and forcing of CCIMS-nwA and model validation. Section 4 presents model results in three applications. The last section presents a summary and conclusions.

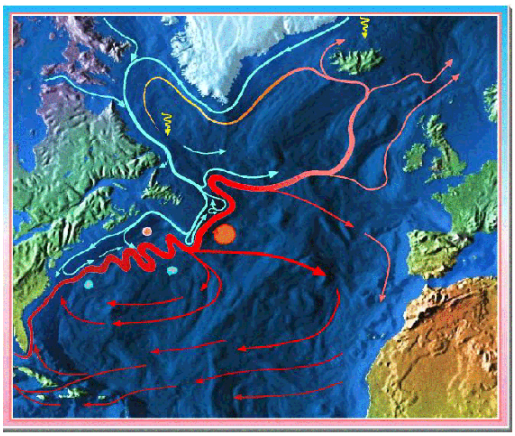

Figure 1. Schematic of surface circulation and main topographic features over the northwest Atlantic Ocean (by courtesy of Dr. Igor Yashayaev, Bedford Institute of Oceanography, Canada).

2. Coupled Circulation-Ice Model

The coupled ocean circulation-sea ice modelling system (CCIMS-nwA) has two

components: (a) the 3D ocean circulation modelling component based on the Regional Ocean Modeling System (ROMS) (Shchepetkin & McWilliams, 2005) and (b) the sea ice modelling component based on the Los Alamos Sea Ice Model (CICE) (Hunke, 2010). ROMS has widely been used in simulating the 3D circulation and hydrography, and two-dimensional (2D) sea levels, through solving the Reynolds-averaged Navier-Strokes equations using terrain-following vertical coordinates (Haidvogel et al., 2008). CICE has widely been used in simulating the sea ice conditions such as the category, concentration, thickness and speed of sea ice by solving numerically the dynamic and thermodynamic equations for multiple ice thickness categories (Hunke et al., 2015). For the two-way coupling between ROMS and CICE, an external coupler (github.com/kshedstrom/roms) is used in the first version of CCIM-nwA and the Model Coupling Toolkit (Jacob et al., 2005) is used in the latest version.

CCIMS-nwA has the nesting capacity with multi-level nested domains of progressively smaller areas with finer horizontal resolutions. Several different versions of CCIM-nwA were used for different applications (Pei et al., 2022; Yang et al., 2023; Sui et al., 2024). The main advantage of the nested-grid modelling setup is that the lower-level submodel with a finer horizontal resolution can better resolve spatial features over a focal area than the upper-level submodel with a coarse horizontal resolution. Several different nested-grid setups for CCIMS-nwA were used in the past based on requirements of different research projects.

Figure 2 shows the first version of CCIMS-nwA with four-level nested-grids for simulating 3D circulation and hydrography over coastal waters of Halifax Harbour (HH) and adjacent coastal waters (Sui et al., 2024). In this nested-grid setup, the outer-most submodel (L1) of CCIMS-nwA covers the ECS and adjacent deep ocean waters of the nwA between 80˚W and 40˚W and between 34˚N and 55˚N (**Figure 2(a)**), with the grid resolution in km to be the same in both the east-west and north-south directions and is equal to the grid spacing in km of 1/12˚ in longitude. Submodel L2 covers the region of the Gulf of St. Lawrence (GSL), Scotian Shelf (ScS), Gulf of Maine (GoM) and adjacent deep waters between 71.5˚W and 56˚W and between 38.5˚N and 52˚N, with a horizontal resolution of 1/36˚ (**Figure 2(b)**). Submodel L3 covers the middle and southwestern areas of the ScS between 66˚W and 63˚W and between 43˚N and 44.75˚N with a horizontal resolution of ~730 m (**Figure 2(c)**). Submodel L4 covers Halifax Harbour (HH) and adjacent waters with a horizontal resolution of about 185 m (**Figure 2(d)**). A one-way nesting technique is used in which the simulated sea levels, currents, temperature, and salinity produced by the upper-level submodel of CCIMS-nwA are used to specify lateral boundary conditions of the lower-level submodel. The model bathymetry for CCIMS-nwA is derived from the 1/240˚-resolution General Bathymetric Chart of the Oceans (GEBCO) 2009 dataset (GEBCO Compilation Group, 2019). In developing a couped physical-BGC modelling system for the nwA, the domain of submodel L1 was extended northward to include the whole Labrador Shelf and Sea, Davis Strait and Baffin Bay (Yang et al., 2023; Ohashi et al., 2024).

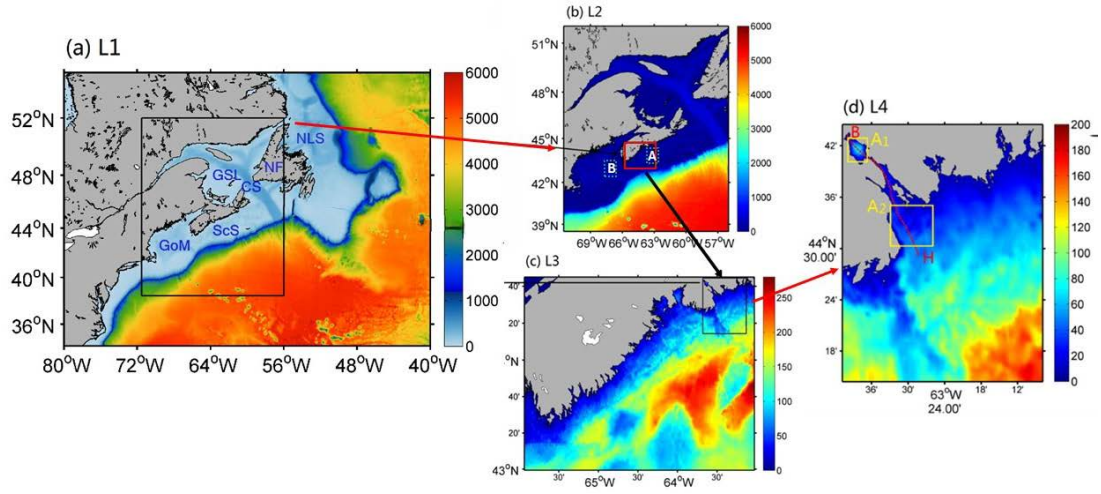

Figure 2. Major topographic features and domains of four submodels for CCIMS-nwA. The horizontal resolutions are 1/12˚, 1/36˚, ~1 km and ~180 m respectively for submodels (a) L1, (b) L2, (c) L3, and (d) L4. Color image in each subplot represents water depths. Abbreviations are used for Newfoundland (NL), Newfoundland Shelf (NLS), the Gulf of St. Lawrence (GSL), Cabot Strait (CS), Scotian Shelf (ScS), and Gulf of Maine (GoM).

For the sub-grid scale mixing parameterizations in each circulation submodel of CCIM-nwA, the Smagorinsky scheme (Smagorinsky, 1963) and the level 2.5 Mellor-Yamada turbulence closure scheme (Mellor & Yamada, 1982) are used for the horizontal and vertical eddy mixing coefficients, respectively. Each circulation submodel uses 40 terrain-following layers (S-layers) in the vertical direction. The initial conditions of temperature, salinity, sea level, and 3D currents are based on the daily mean Global Ocean Physics Reanalysis dataset (GLORYS, Lellouche et al., 2021), which has a horizontal resolution of 1/12˚. This dataset was constructed by the Copernicus-Marine Environment Monitoring Service (CMEMS; resources.marine.copernicus.eu).

Model external forcing for driving CCIMS-nwA includes (a) atmospheric forcing specified at the sea (or ice) surface, (b) tides, ice conditions and inflows specified at the open boundaries of L1, (c) riverine freshwater discharges, and (d) continental runoff due to melting of ice and snow over land. Atmospheric forcing includes the three-hourly fields of air pressure, specific humidity, temperature, shortwave, longwave radiation fluxes, cloud fraction, and precipitation, and three-hourly winds at 10 m above the mean sea level. These three-hourly fields were extracted from the three-hourly North American Regional Reanalysis (Mesinger et al., 2006), which has a horizontal resolution of 32 km.

A combination of two types of open boundary conditions (OBCs) is specified at the lateral open boundaries of submodel L1, using the adaptive open boundary condition of Marchesiello et al. (2001). The first type is tidal forcing expressed in terms of tidal sea levels and depth-mean currents of 11 major tidal constituents (M_2, S_2, N_2, K_2, K_1, O_1, P_1, Q_1, M_4, MS_4, and MN_4). The harmonic constants of these tidal constituents were extracted from the regional solution for the Atlantic Ocean of the Oregon State University Tidal Inversion System (Egbert and Erofeeva, 2002) with a horizontal resolution of 1/12˚. The second

type of OBCs is daily-mean temperature and salinity and non-tidal elevations and currents derived from GLORYS.

Freshwater discharges from 49 major rivers over the ECS are specified as volume flux through the bottom of a model grid cell in the CCIMS-nwA. Each river in the model is represented by a channel normal to the model's coastline. The temperature at the head of each river is set to the GLORYS sea surface temperature at the grid point closest to the river mouth. The freshwater discharge from the St. Lawrence River is specified using the monthly-mean discharge at Quebec City estimated by the St. Lawrence Global Observatory using the regression model of Bourgault & Koutitonsky (1999). For rivers in Canada other than the St. Lawrence, monthly-mean discharge observations were obtained from the websites of the Water Survey of Canada and the United States Geological Survey.

3. Model Validation

To assess the model performance, results produced by CCIMS-nwA in 2018 are compared with various types of oceanographic observations. Time series of observed and simulated total sea surface elevations at Yarmouth of Nova Scotia are shown in **Figure 3(a)** for the period of February and March 2018. For quantitative assessments of the model skill, the γ^2 value suggested by Thompson and Sheng (1997) is used:

$$\gamma^2 = \frac{Var\left(X_o - X_m\right)}{Var\left(X_o\right)} \tag{1}$$

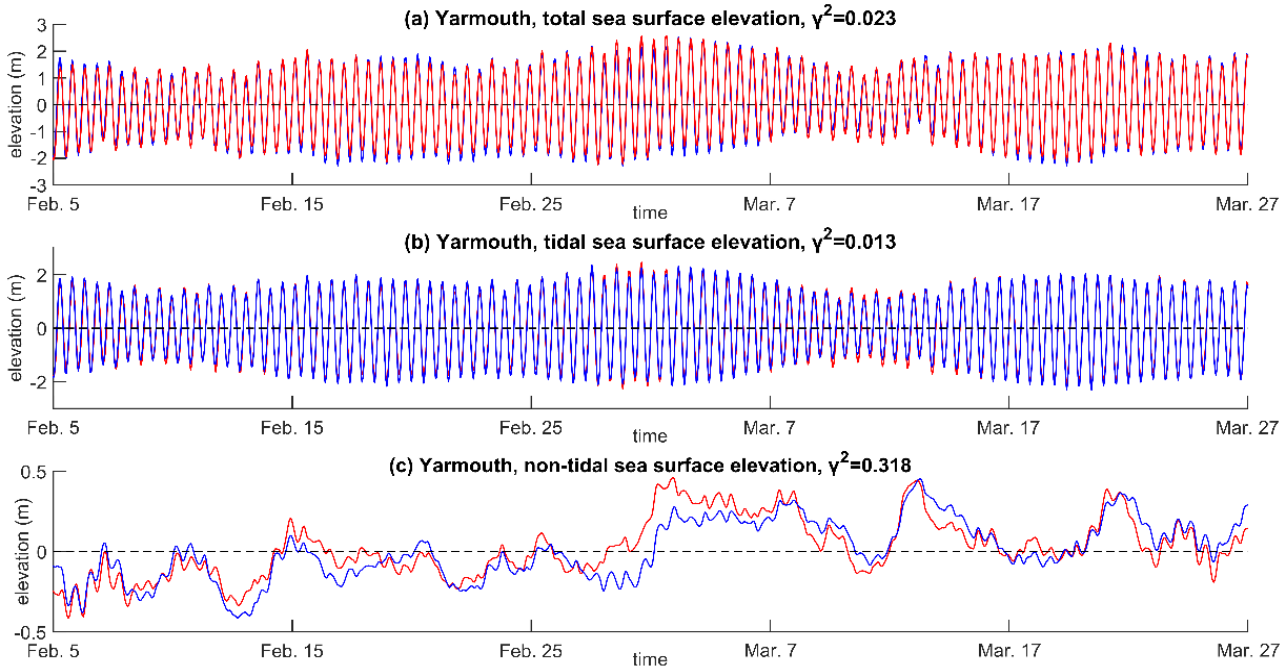

Figure 3. Time series of observed (red) and simulated (blue) (a) total, (b) tidal and (c) non-tidal surface elevations at Yarmouth tidal gauge station from 5 February to 27 March 2018. The simulated results are produced by L1.

where X_m and X_o represent respectively the simulated and observed value of variable X at the same observation time. The γ^2 values are in the range of 0 and infinity. Smaller values of γ^2 imply better performances of the numerical model in simulating variable X. The critical value of γ^2 is set to 1 in this study. As shown in **Figure 3(a)**, L1 reproduces very well the observed total surface elevations at Yarmouth, with the γ^2 value of ~0.023.

The total sea surface elevations are driven by tidal and non-tidal forcing. To examine the model performance in simulating tidal and non-tidal components of sea surface elevations, the observed and simulated total sea surface elevations are decomposed into tidal and non-tidal components using Matlab program t_tide (Pawlowicz et al., 2002). It should be noted that the non-tidal surface elevations obtained by using t_tide still contain some weak tidal components. As a result, any remaining high-frequency variability with periods of less than 3 hours in the non-tidal surface elevations is eliminated using a low-passed filter. As shown in **Figure 3(b)** and **Figure 3(c)**, L1 performs reasonably well in simulating tidal and non-tidal surface elevations at Yarmouth, with the small γ^2 values of ~0.01 and ~0.32, respectively. It should be noted that the model skill in simulating non-tidal surface elevations (or storm surge) is affected significantly by the accuracy of atmospheric forcing and also the horizontal resolution of the model.

In addition to the satisfactory skill of L1 at Yarmouth shown in **Figure 3**, Pei et al. (2022) and Yang et al. (2023) demonstrated that L1 has very satisfactory skill in simulating the tidal and non-tidal surface elevations at tide gauge stations in Nain, Bonavista, North Sydney, Halifax, and Saint John.

As shown in Pei et al. (2022) and Sui et al. (2024), CCIMS-nwA also has satisfactory skills in simulating the temporal variability of temperature and salinity over the ECS. To demonstrate the model skill in simulating the observed seasonal cycles of hydrography, time series of simulated and satellite observed daily SSTs averaged over two dashed green boxes marked by labels A and B in **Figure 2(b)** in the southwestern Scotian Shelf (swScS) and central Gulf of Maine (cGOM) are shown in **Figure 4** respectively. The simulated SSTs were produced by L2. The satellite SST data were extracted from daily GHRSST Level 4 CMC0.1deg Group for High Resolution Sea Surface Temperature Analysis (https://www.ghrsst.org/).

Over the swScS (**Figure 4(a)**), the daily satellite observed SSTs were low and less than 6.0˚C in the first three months of 2018 due mainly to the negative net heat fluxes at the sea surface in winter. The observed SSTs became warmer from year-day 120 to 220 due mainly to the positive net surface heat flux from early spring to late summer. After reaching the maximum of ~21.0˚C, the daily observed SSTs decreased to ~4.0˚C mainly due to the negative surface heat fluxes. Due to the above-mentioned seasonal variations in the net surface heat flux, the daily satellite observed SSTs over the cGoM decreased gradually from ~9.0˚C to 5.0˚C in the first 70-year days of 2018 and then increased with time in spring and summer (**Figure 4(b)**). After reaching the maximum of ~20.0˚C, the observed SSTs over the cGoM got colder from the late summer to the end of fall. The simulated SSTs produced by L2 are in good agreement with the satellite

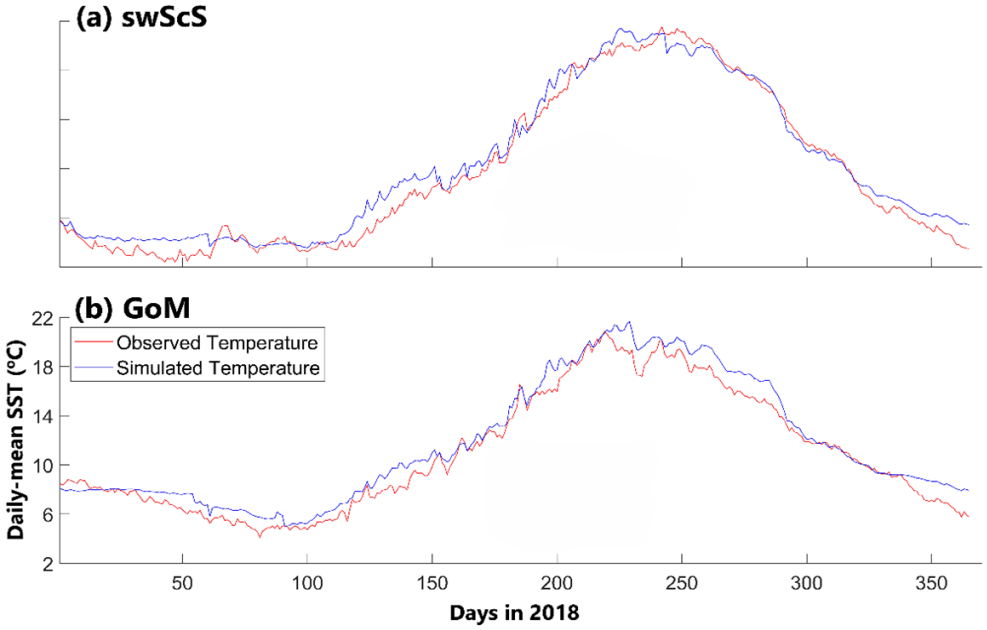

Figure 4. Time series of daily-mean SSTs produced by L2 in 2018 (blue lines) averaged over green dashed boxes over (a) the swScS and (b) cGoM. The red lines represent the time series of remote sensing SST observations extracted from the daily GHRSST (Pei et al., 2022).

observed SSTs over the swScS and cGoM (**Figure 4**). In comparison with the satellite SST data, the simulated SST produced by L2 has the correlation square of ~0.99 (0.98), γ^2 value of ~0.017 (0.021), and the root mean square error (RMSE) of 0.81˚C (0.70˚C) over the swScS (cGoM).

We next assess the performance of CCIMS-nwA in simulating 3D currents and temperature by comparing results produced by L3 with the GLORYS dataset. Previous studies demonstrated that GLORYS represents reasonably well the observed distributions and variability of 3D large-scale currents and hydrography in the global ocean (Lellouche et al., 2021). The February-mean SSTs produced by L3 in 2014 range from −2.0˚C to 1.0˚C over the inner shelf and from ~2.0˚C to 4.0˚C in the offshore waters of the swScS (**Figure 5(a)**). In several bays, the February-mean SSTs are low due mainly to the smaller heat storage over coastal shallow waters than in the offshore deep waters (Sui et al., 2024). The Nova Scotia Current (NSC) flows southwestward from the middle area of the swScS through the northern area of the eastern open boundary of L3 (**Figure 5(a)**), with a narrow and weak northeastward jet over the inner shelf driven mainly by local winds. In comparison, the February-mean GLORYS does not have the cool SST over the inner shelf and fine-scale circulation features over the southwestern area of the L3 domain (**Figure 5(b)**), due mainly to the coarse horizontal resolution of GLORYS and tidal forcing.

In July, the monthly mean simulated SST ranges between 10.0˚C and 20.0˚C over the inner shelf and ranges between 12.0˚C and 15.0˚C in the offshore waters of the swScS (**Figure 5(c)**). In several coastal embayments, the July-mean SSTs are relatively warm, due again to the small heat storage over shallow waters. The

July-mean SSTs are relatively cool (about 8.0˚C) over the coastal area off Cape Sable, caused by strong tidal mixing that blends cold deep waters with the warmer surface waters. An intense northeastward coastal jet in this month occurs over the inner shelf of the swSCS (**Figure 5(c)**). This inshore jet in July is driven mainly by the strong southwesterly winds. The persistent southwesterly winds in summer lead to relatively cool SST over the inner shelf, due mainly to coastal upwelling and vertical mixing (Pei et al., 2022). By comparison, the July-mean GLORYS also has cool SST and an inshore northeastward jet along the coast over the inshore waters (**Figure 5(d)**). Large differences between L3 and GLORYS SSTs occur over the coastal area of Cape Sable Island. The plausible reasons for these large differences include: the horizontal resolution of the GLORYS dataset is not fine enough to resolve fine-scale topographic and circulation features over the swSCS and the tidal currents and mixing were not included in the GLORYS. For the comparison between SST produced by L3 and GLORYS over the L3 domain, the relative bias (RB) is ~21.6% (~3.5%) and RMSE is ~1.0˚C (~1.3˚C) in February (July) 2014 (Sui et al., 2024).

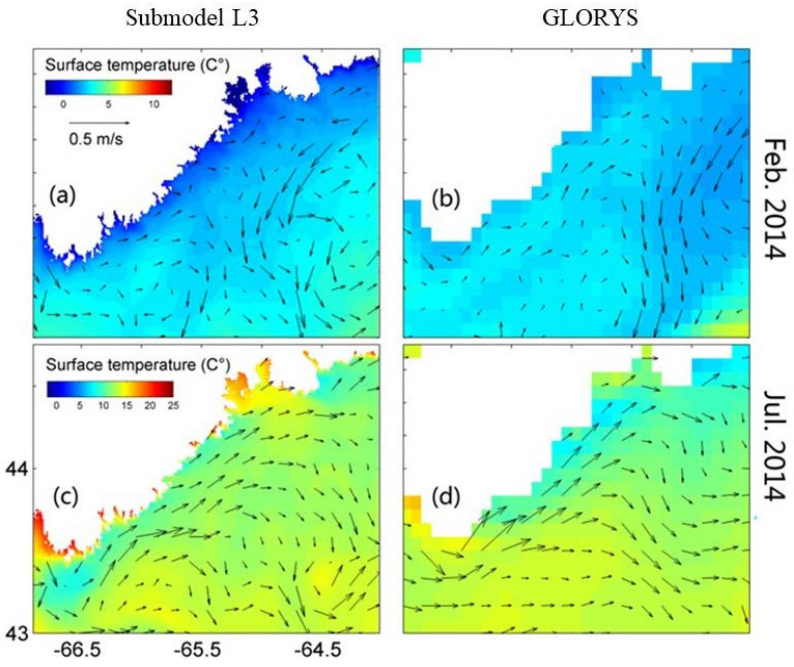

Figure 5. Monthly mean temperature and currents at the sea surface in (a), (b) February and (c), (d) July 2014 calculated from results generated by (a), (c) submodel L3 and (b), (d) GLORYS. For clarity, velocity vectors are plotted at every 16th model grid point (Sui et al., 2024).

The February-mean sub-surface (50 m) temperature produced by L3 ranges between 2.0˚C and 5.0˚C over the inner shelf and between 6.0˚C and 7.0˚C over the offshore waters of the swScS (**Figure 6(a)**). The February-mean sub-surface (50 m) currents produced by L3 are relatively strong and southwestward in the offshore areas off about 60 km from the coast and relatively weak over other areas. The July-mean sub-surface temperature produced by L3 are relatively

uniform and between 6.0˚C and 8.0˚C (**Figure 6(c)**), with relatively weak sub-surface currents over the swScS except for a recirculation gyre near the southeastern corner of the L3 model domain.

In comparison with L3 model results, the February-mean GLORYS temperature at 50 m is relatively cold and about 2.0˚C along the main path of the NSC, relatively warm and about 5.0˚C near the coast and about 5.0˚C near the southeastern corner of L3 model domain (**Figure 6(b)**). The February-mean GLORYS sub-surface circulation features a strong and southwestward jet in the offshore areas. The July-mean GLORYS temperature at 50 m shows the relatively lower temperature of about 5.0˚Cin the offshore waters of the swScS and relatively higher temperature of about 7.0˚C over Cape Sable (**Figure 6(d)**).The July-mean GLORYS currents at 50 m run northeastward over the inner shelf and southwestward over the offshore waters. For the comparison between L3 and GLORYS sub-surface temperature, the RB is ~18% (~15%) and RMSE is ~1.18˚C (~1.15˚C) in February (July) 2014 (Sui et al., 2024).

Readers are referred to Pei et al. (2022), Yang et al. (2023), Sui et al. (2024) and Ohashi et al. (2024) for more assessment of performances of CCIMS-nwA in simulating 3D currents and hydrography over the ECS.

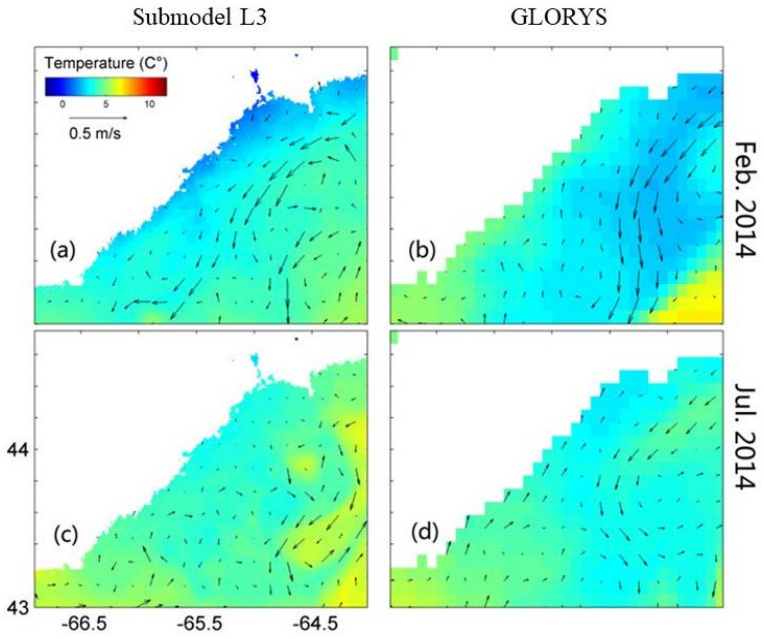

Figure 6. Monthly mean temperature and currents at 50 m in (a), (b) February and (c), (d) July 2014 calculated from results generated by (a), (c) submodel L3 and (b), (d) GLORYS. Otherwise as in **Figure 5**.

4. Model Results in Three Applications

The newly-developed CCIMS-nwA has been used in several research projects, including (a) construction of a coupled physical-biogeochemical modelling system for the nwA (Ohashi et al., 2024), (b) examination of tide-surge interactions over the ECS (Yang et al., 2023), (c) quantification of hydrodynamics and con-

nectivity among the marine protected areas on the ScS, (d) high-resolution simulations of circulation and dissolved oxygen in coastal waters, (e) examination of circulation and residence time in the Bras d'Or Lake, and (f) investigation of low-salinity waters over the ECS. Model results in the last three applications are examined in this section.

4.1. Seasonal Variability of Circulation and Dissolved Oxygen in Halifax Harbour

The four-level nested-grid setup of CCIMS-nwA shown in **Figure 2** was recently used in simulating 3D circulation and hydrography in the Halifax Harbour (HH) and adjacent waters. Model results produced by L4 with the horizontal resolution of 185 m were used in examining the sporadic landward intrusion of offshore sub-surface high-salinity waters into Bedford Basin (BB) through HH (Sui et al., 2024). L4 was also coupled to a simple dissolved oxygen model (L4COM) in simulating the time-dependent and 3D distribution of dissolved oxygen (DO) in HH and BB. The monthly mean circulation, salinity and DO produced by L4COM are examined here.

In February, the monthly mean simulated near-surface salinity at 2 m gradually increases from about 25.0 near the mouth of the Sackville River to about 32.0 in the outer Harbour (OH) (**Figure 7(a)**), due mainly to freshwater discharges from the Sackville River and sewage outflows in HH. The near-surface salinity is also low and about 30.0 in Northwest Arm. The monthly mean near-surface currents in February are mainly seaward (southeastward) in BB, the Narrows, and inner Harbour (IH) (**Figure 7(a)**).

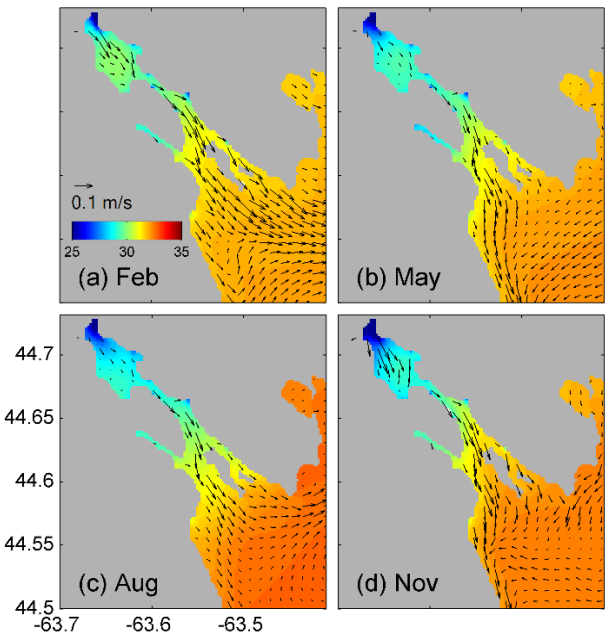

Figure 7. Monthly mean near-surface salinity and currents at 2 m in (a) February, (b) May, (c) August and (d) November 2014 in Halifax Harbour and adjacent waters calculated by L4COM.

In May, the monthly mean near-surface salinity in BB is about 29.0, which is lower than the counterpart in February (**Figure 7(b)**), due mainly to large freshwater discharges associated with ice and snow melt and relatively weak vertical mixing in spring. In BB, the monthly mean near-surface currents in May are seaward and relatively weaker than the counterparts in February. Over the IH and OH, the monthly-mean near-surface salinity in May is highly similar to the counterpart in February. The May-mean near-surface currents are also seaward, with a narrow and southward jet along the west coast of the OH.

In August, the monthly mean near-surface (2 m) salinity in BB is also relatively low and about 28, due to the large freshwater discharges associated with large precipitation in the summer (**Figure 7(c)**). In the OH, the monthly mean near-surface salinity in this month is about 32.5, which is slightly higher than the counterparts in February and in May. One of the plausible reasons is the northward near-surface wind-driven currents, which transport the relatively salty coastal waters from the inner ScS into the OH.

In November, the monthly mean near-surface salinity in BB is about 27 and the lowest among these four months (**Figure 7(d)**), due mainly to the significantly large freshwater discharges from the Sackville River and sewage outflows. The monthly mean near-surface seaward currents are relatively large in this month, due mainly to the large freshwater discharges from the Sackville River (**Figure 7(d)**).

We next examine the seasonal variations of simulated DO produced by L4COM. The monthly mean simulated near-surface DO in February is relatively high and ranges between 350 mmol·m^{-3} in BB and 310 mmol·m^{-3} in the OH (**Figure 8(a)**). In May, the monthly mean near-surface DO in BB is about 330 mmol·m^{-3} due to the relatively warmer SST in spring than in winter, which decreases the DO solubility (**Figure 8(b)**). Meanwhile, the monthly mean

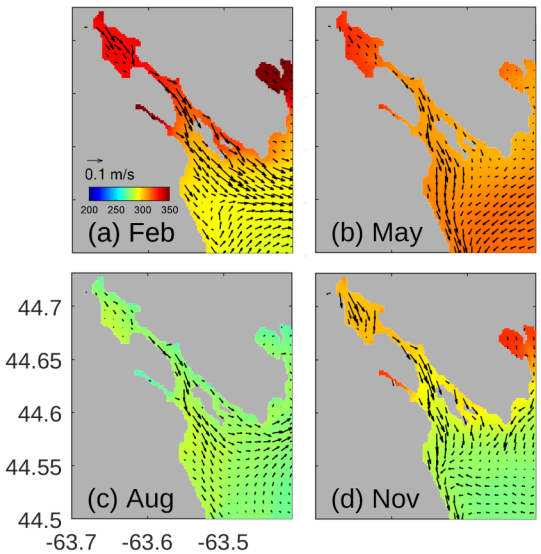

Figure 8. Monthly mean near-surface DO (mmol·m^{-3}) and currents at 2 m in 2014 in Halifax Harbour and adjacent waters calculated from model results produced by L4COM.

near-surface DO in the OH slightly increases to 320 mmol·m^{-3} due to the southwestward flows with high DO from the offshore waters. The monthly mean near-surface DO in HH is relatively low and about 280 mmol·m^{-3} (**Figure 8(c)**), due to the relatively warm SST in summer. In November, the monthly mean near-surface DO in BB increases to 310 mmol·m^{-3} associated with cold SST (**Figure 8(d)**).

Two intense intrusion events of offshore sub-surface high-salinity waters flowing into the lower layers of BB were examined by Sui et al. (2024). To examine the variability of DO during those two intense intrusion events, the simulated instantaneous DO along the longitudinal transect BH (**Figure 2(d)**) produced by L4COM is considered. Before the start of this intense intrusion event (**Figure 9(a)**), the DO in the surface layer in HH gradually decreases from about 330 mmol·m^{-3} in BB to about 280 mmol·m^{-3} in the OH. In the BB, DO gradually decreases from about 330 mmol·m^{-3} in the surface layer to about 270 mmol·m^{-3} at the bottom of BB. DO is significantly affected by the joint effect of solubility of dissolved oxygen, air-sea oxygen flux, vertical mixing, and advection in HH.

When the intrusion event starts around 23:00 on 3 February, the relatively high-DO waters with the upper boundary marked by the contour line of 280 mmol·m^{-3} sink to deep layer of BB and reach the bottom over the southeastern flank of BB (**Figure 9(b)**). This indicates the downslope movement of high-DO waters from the surface layer to the bottom of BB. During the intrusion event

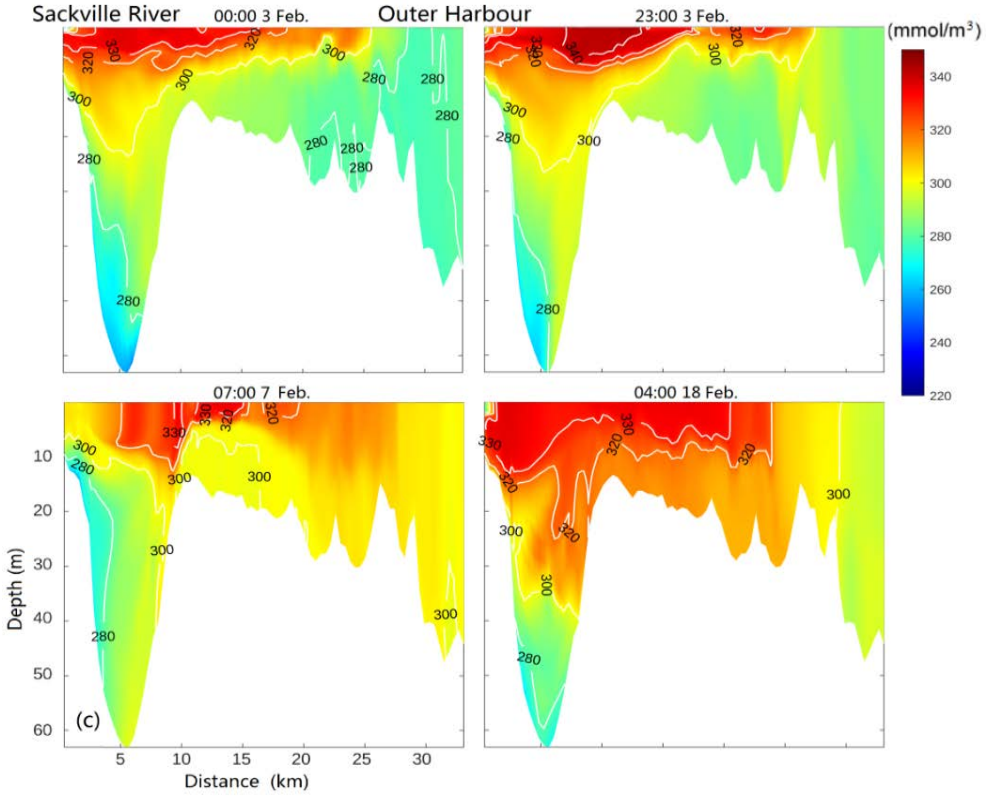

Figure 9. Vertical distribution of DO along the longitudinal transect BH at (a) 00:00 on 3, (b) 23:00 on 3, (c) 7:00 on 7, and (d) 4:00 on 18 February 2014 based on results produced by L4COM.

(**Figure 9(c)**), the relatively high-DO waters enter the lower water column of BB. At this time, high-DO waters with the upper boundary marked by the contour line of 300 mmol·m^{-3} sink to middle layer of BB near the Narrows. DO in the deeper waters of BB increases to about 290 mmol·m^{-3}. After the intrusion event (**Figure 9(d)**), the DO in the BB is higher than the counterpart before the intrusion event.

Before the start of the second intrusion event (not shown), DO in the surface layer in HH gradually decreases from about 300 mmol·m^{-3} in BB to about 250 mmol·m^{-3} in the OH. DO in BB at this time has different features in four layers, which consist of a thin surface layer with relatively high DO about 300 mmol·m^{-3}, an upper intermediate layer with relatively low DO between 280 to 290 mmol·m^{-3}, a lower intermediate layer with relatively high DO about 310 mmol·m^{-3}, and a bottom layer with low DO between 250 to 290 mmol·m^{-3}. When the second intense intrusion event starts around 7:00 on 3 July, the relatively low-DO waters intrude from the OH to the lower water column of IH (not shown). During the intrusion event, the relatively low-DO waters intrude from the OH and enter BB. Over the southeastern flank of BB, DO in the lower intermediate layer at this time is about 280 mmol·m^{-3} and lower than the counterpart before the intrusion event. After the intrusion event, the low-DO waters from the OH gradually retreat from BB to the Narrows at 10:00 on 23 July. DO in the bottom layer of BB at this time is lower than the counterpart before the intrusion event.

4.2. Circulation and Residence Time in the Bras d'Or Lake

Bras d'Or Lake (BdOL) in northeastern Nova Scotia of Canada is a salty inland lake, with a surface area of ~1100 km^2 and the maximum water depth of 287 m. The Lake is connected to the Gulf of St. Lawrence by the Great Bras d'Or Channel (GBDC) and Little Bras d'Or Channel (LBDC). Freshwater input from rivers around the Lakes makes the BdOL to be a unique and very productive natural habitat. The Lake was designated as a UNESCO Biosphere Reserve in 2011. Economic activities such as fisheries and aquaculture in the BdOL require better understanding of retention and hydrodynamic connectivity in the Lake.

As part of a collaborative research project known as Mapping and Modelling the dead zones of the Bras d'Or Lake estuary in the context of Aquaculture development, a 3-level nested grid modelling system known as CCIMS-BdOL was developed (**Figure 10**). The domain of submodel L1 (**Figure 10(a)**) is larger than the one shown in **Figure 2(a)**, due to our recent upgrading of the nested-grid modelling system. Submodel L2 (**Figure 10(b)**) covers the southern GSL, eastern ScS and adjacent deep ocean waters, with a horizontal resolution of about 2 km. Submodel L3 (**Figure 10(c)**) covers the BdOL with a horizontal resolution of about 700 m.

Model results produced by L3 in 2019 are considered in this section. **Figure 11** shows that L3 has satisfactory skill in reproducing the seasonal variations of near-surface temperature at three stations (Dundee, St. Peter's Inlet and Whycocomagh Bay) over the southwestern BdOL.

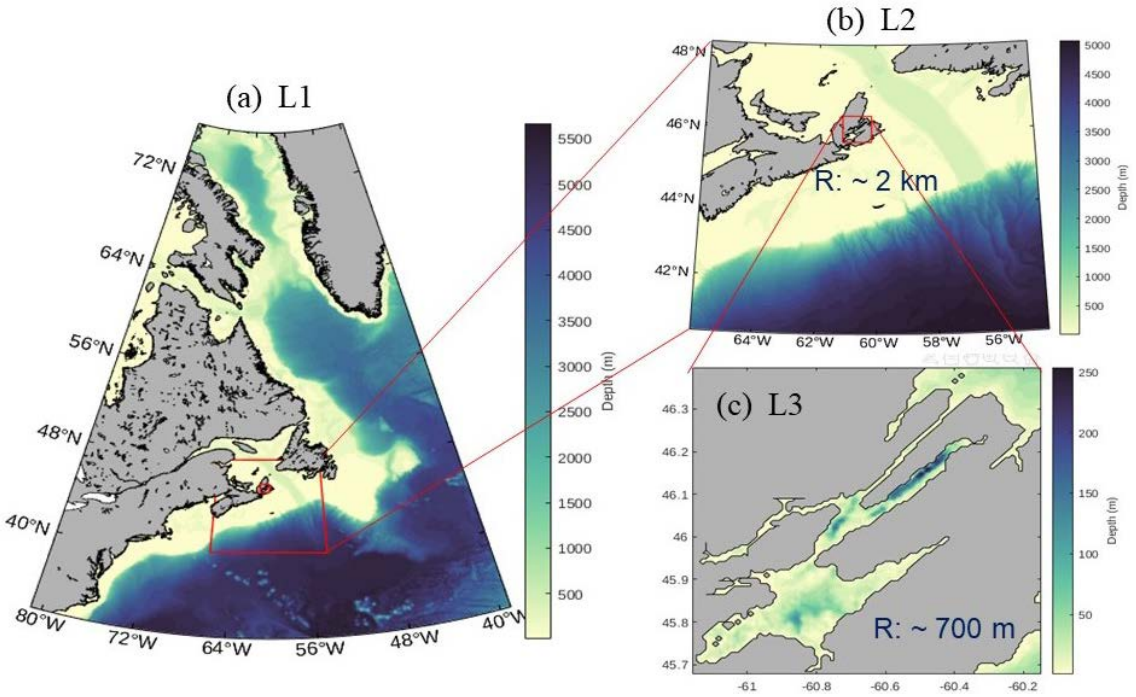

Figure 10. Major topographic features and domains of three submodels for CCIMS-BdOL. The horizontal resolutions are 1/12˚, ~2 km and ~180 m respectively for submodels (a) L1, (b) L2, and (c) L3 respectively. Colour image represents water depths.

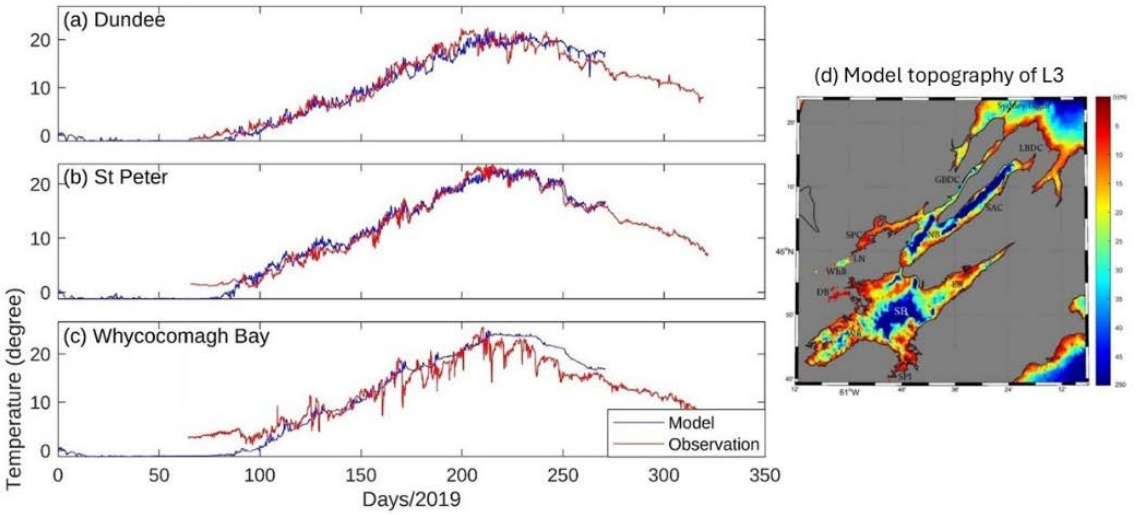

Figure 11. Time series of observed (red line) and simulated (blue) near-surface temperature at (a) Dundee, (b) St. Peter's Inet and (c) Whycocomagh Bay in 2019. Abbreviations are used in (d) for Great Bras d'Or Channel (GBDC), Little Bras d'Or Channel (LBDC), St. Andrew's Channel (SAC), St. Patrick's Channel (SPC), North Basin (NB), Little Narrows (LN), Whycocomagh Bay (WhB), Denys Basin (DB), South Basin (SB), East Bay (EB), West Bay (WB) and St. Peter's Inlet (SPI).

Some noticeable differences occur between the observed and simulated surface temperatures in the synoptic time scales, particularly at Whycocomagh Bay, due mainly to the coarse-resolution atmospheric forcing (ERA5, https://www.ecmwf.int/en/forecasts/dataset/ecmwf-reanalysis-v5) used in driv-

ing CCIMS-BdOL.

The simulated lake surface temperature produced by L3 has large seasonal variability influenced significantly by the net heat flux and freshwater discharges. Local winds also play a very important role, particularly during the ice-free period. The February-mean surface temperature (**Figure 12(a)**) is cold and around −1.0˚C over the South Basin (SB), relatively warm about 2.0˚C in St. Andrew's Channel (SAC) and around 1.0˚C in North Basin (NB) and adjacent waters. The February-mean surface currents are strong and "seaward" associated with the two-layer estuarine circulation from St. Patrick's Channel (SPC) to St. Andrew's Channel (SAC) and relatively weak and nearly uniform in the South Basin (**Figure 12(a)**). It should be noted that the lake ice occurred in the BdOL from late January to the end of March in 2019, with the most lake surface covered by ice in the second half of February and first half of March.

In May, the monthly mean surface temperature (**Figure 12(b)**) is relatively warm and about 7.0˚C - 8.0˚C over shallow bays including Denys Bay (DB), Whycocomagh Bay (WhB), Little Narrow (LN), SPC, and St. Peter's Inlet (SPI), and relatively cold and about 4.0˚C - 5.0˚C over the SB, NB and SAC. The May-mean surface currents are strong and also seaward over areas from SPC to SAC, with a cyclonic gyre over the western part of the SB.

In August, the monthly mean surface temperature is warm and about 21.0˚C - 24.0˚C over the shallow bays of DB, WhB, SPC, SPI and EB, and relatively cooler and about 15.0˚C - 17.0˚C over the NB and SAC (**Figure 12(c)**). The August-mean surface currents feature a strong cyclonic circulation over the central

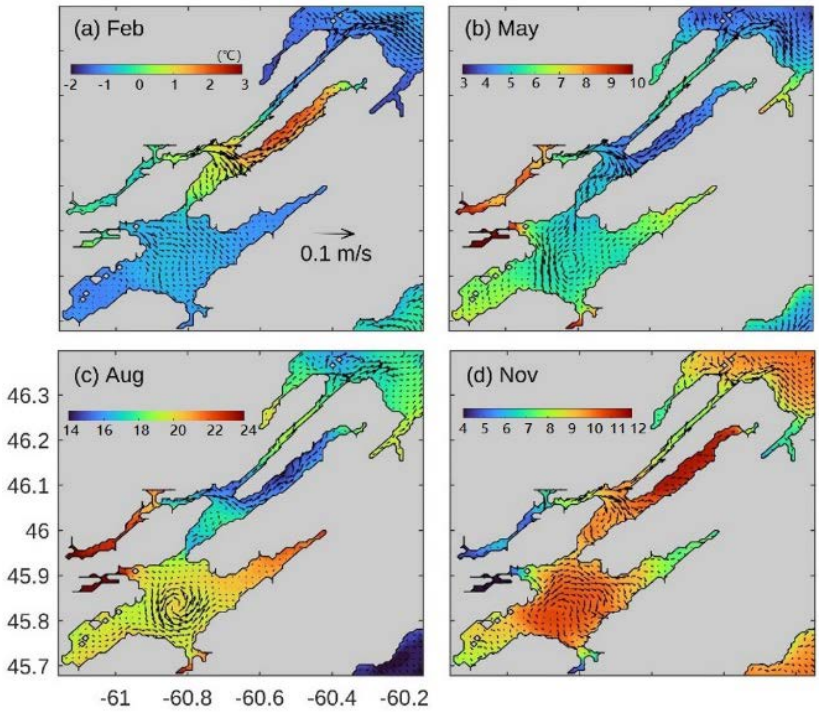

Figure 12. Monthly mean surface currents and temperature in (a) February), (b) May, (c) August and (d) November 2019 in the Bras d'Or Lake produced by L3 of CCIMS-BdOl.

area of the SB, and relatively strong and seaward from SPC to SAC.

The November-mean surface temperature is relatively cool and about 6.0˚C - 8.0˚C in the shallow bays and relatively warm and about 10.0˚C - 12.0˚C in the NB, SAC and SB (**Figure 12(d)**). The November-mean surface currents have very similar circulation features from SPC to SAC as in February and May, but are strong and anticyclonic over the SB.

To quantify the residence time in the BdOL, the numerical particle-tracking program known as ROMSPath (Hunter et al., 2022) is used to calculate movements of passive particles carried by the annual mean currents in 2019 produced by L3 of CCIMS-BdOL. The number of particles remaining in a given release area (including particles that exited but returned to the release area) are counted. This number is normalized by the number of particles released, resulting in a time series of the fraction of released particles that is in the release area. The MATLAB's Curve Fitting Toolbox is then used to determine the e-folding time (τ) by fitting an exponential decay function to each experimental curve. By defining the residence time (T_r) to be the time by which only 10% of total particles remains over the release area, we have $T_r = 2.3\tau$.

For particles released in the surface waters in the BdOL, the residence times estimated using the annual-mean currents in 2019 (**Figure 13(a)**) are short and about 5 days in SPC, 7 - 10 days in SPI, NB and WB, and relatively long and about 17 days in the GBDC, 33 days in LN and 85 days in WhB. For paticles near the bottom of the BdOL, the residence times in 2019 (**Figure 13(b)**) are longer and about 15 - 16 days in SPC and SPI, 33 days in LN, 58 days in WB, 139 days in the GBDC and 233 days in WhB.

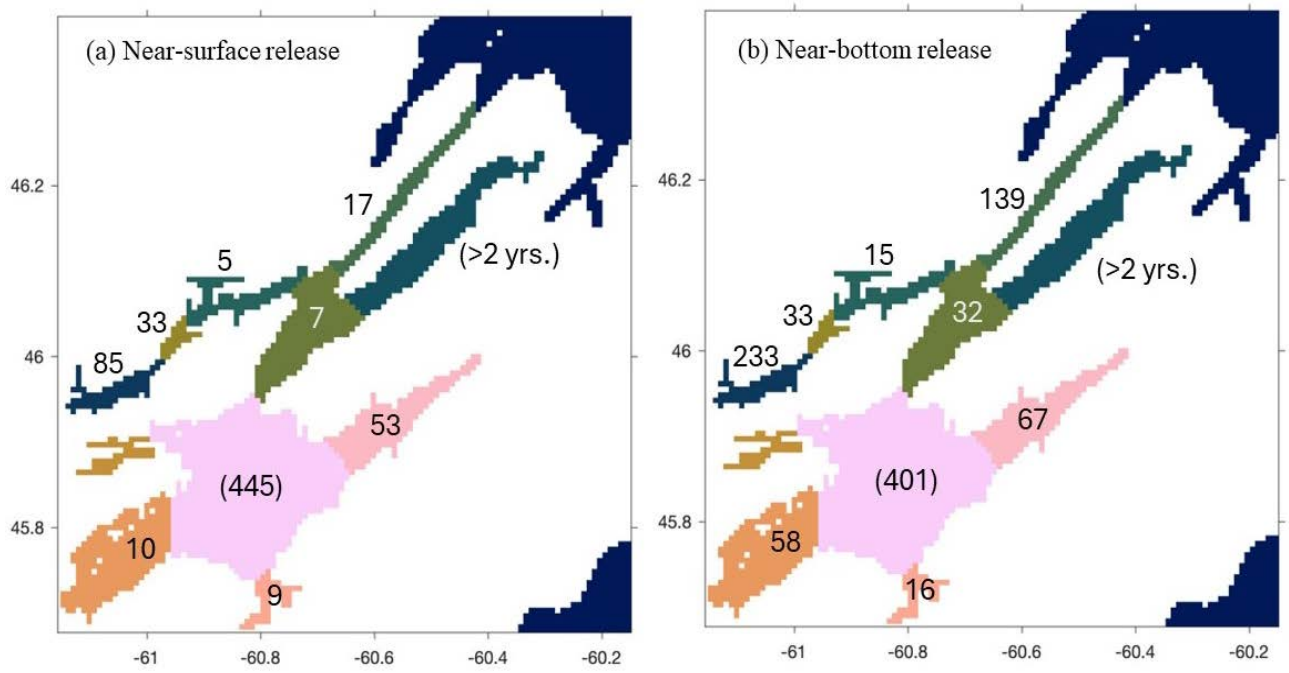

Figure 13. Residence times (in days) estimated from particle-tracking experiments using the annual mean simulated currents, with particles released a) near the surface and b) near the bottom.

4.3. Freshwater Fluxes over the ECS

The 3D circulation and hydrodynamics over the ECS are affected significantly by freshwater input from land, rivers and high-latitude ice melting. Freshwater flux also plays a very important role in the formation of water masses over the ECS. Model results produced by L1 of CCIMS-BdOL during the 5-year period 2014-2018 are analyzed to determine the spatio-temporal variability of freshwater thickness (H_f) and flux ($\vec{U}_f$) on the ECS. We follow Wang et al. (2022) and define

$$H_f = \int_{-Z_o}^{\eta} \left(S_0 - S\right)/S_0 dz \tag{2}$$

$$\vec{U}_f = \int_{-Z_o}^{\eta} \vec{U}\left(S_0 - S\right)/S_0 dz \tag{3}$$

where S_0 = 35.5 is the reference salinity, η is the sea surface, Z_o is set to 100 m, and $\vec{U}$ is time-dependent 3D currents produced by L1 of CCIMS-BdOL.

The monthly mean freshwater thickness in April averaged over the 5-year period has large spatial variability over the ECS and is near zero in the deep ocean waters of the nwA (**Figure 14(a)**). The April-mean freshwater thickness is greater 8 m over the shelf break and inner shelf of the Labrador Shelf (LS) and the northern Newfoundland Shelf (nNF) due mainly to the equatorward transport of low-salinity waters through the northern open boundary of L1. Over these two regions, the April-mean freshwater flux is intense and mostly equatorward over both the shelf break and inner shelf areas (**Figure 14(a)**). Around the southern tip of Grand Banks (GBs), part of equatorward freshwater flux turns cyclonically and flows polarward into the deep waters off the shelf break of the eastern NF. Due mainly to the freshwater runoff from the St. Lawence River, the April mean freshwater thickness is about 10 m with the southeastward (seaward) freshwater flux in the deep water areas of the Gulf of St. Lawrence (GSL) and Laurentian Channel (LC). On the inner shelf areas of the Scotian Shelf (ScS) and northeastern Gulf of Maine (neGoM), the April mean freshwater thickness is also large and about 10 m, with the equatorward flux in the top 100 m. Over the shelf break of the ScS and GoM, the April mean freshwater thickness is relatively thin, but with intense equatorward flux in the top 100 m.

The October-mean freshwater thickness is also relatively large with large spatial variability over the ECS and near zero in the deep ocean waters (**Figure 14(b)**). Over the inner shelf and shelf break areas of the LS and nNF, the October-mean freshwater thickness is larger and about 12 m with stronger equatorward freshwater flux, in comparison with the April-mean values. Over the GSL and inner shelf of the ScS, the October-mean freshwater thickness is about 12 m, which is larger than the April-mean values. By contrast, the October-mean freshwater thickness is about 6 m over the inner shelf areas of the neGoM, which is significantly smaller than the April-mean values.

To examine the main physical processes affecting the spatio-temporal variability of the freshwater flux, the Empirical Orthogonal Function (EOF) analysis is conducted for the monthly anomaly of $\vec{U}_f$, which is calculated by subtracting

the 5-year mean of monthly means from the monthly mean fluxes in the top 100 m in each year. The spatial patterns and time-dependent coefficients for the first two EOFs are shown in **Figure 15**. These two EOFs explain respectively about 22% and 10% of the total variance respectively. Over the LS and nNF, the EOF1 has large along-isobath fluxes in the top 100 m over the shelf break and relatively

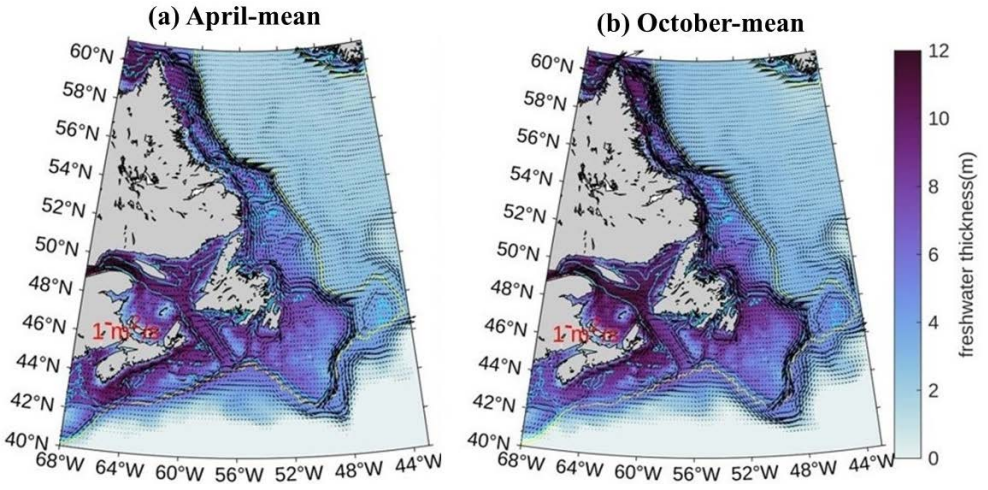

Figure 14. Monthly mean freshwater thickness (image) and flux (vectors) in the top 100 m (a) April and (b) October over the ECS and adjacent deep ocean waters based on results produced by L1 during the 5-year period 2014-2018.

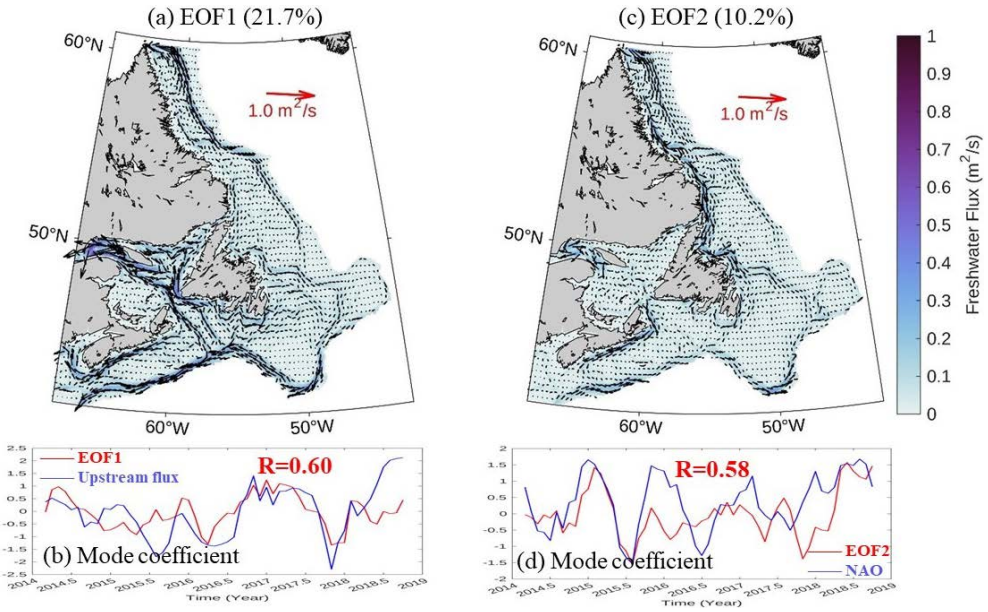

Figure 15. Patterns and coefficients of monthly anomaly of freshwater flux in the top 100 m for the (a), (b) first and (c), (d) second EOFs based on results produced by L1 during the 5-year period 2014-2018.

weak values on the inner shelf (**Figure 15(a)**). Over the nNF, EOF1 has relatively large along-isobath freshwater fluxes over the northern flank of the nNF. This along-isobath flux joins the strong flux at the shelf break of eastern NF. Over the

inner shelf and shelf break of GBs and ScS, EOF1 has large along-isobath freshwater flux. In the GSL, EOF1 has large fluxes in the deep channels. The cross-correlation coefficient analysis shows that time-dependent mode coefficient of EOF1 is correlated with the upstream freshwater flux specified at the northern open boundary of L1 (**Figure 15(b)**), with the correlation coefficient of about 0.60.

In comparison with EOF1, the mode of EOF2 has relatively large along-isobath fluxes over the inner shelf and shelf break of the LS (**Figure 15(c)**). Over the NF and GBs, EOF2 has similar along-isobath fluxes over the shelf break, but much weaker fluxes over the inner shelf than EOF1. The time-dependent coefficient of EOF2 is correlated with the North Atlantic Oscillation (NAO), with the correlation coefficient of about 0.58 (**Figure 15(d)**).

5. Summary and Conclusions

A fully coupled ocean circulation-sea ice modelling system (CCIMS-nwA) with the multi-grid nesting capacity was developed for the coastal and shelf waters of the northwest Atlantic. CCIMS-nwA was based on the Regional Ocean Modeling System (ROMS) and Los Alamos Sea Ice Model (CICE). CCIMS-nwA was calibrated extensively in the past (Pei el al., 2022; Yang et al., 2023; Sui et al., 2024; Ohashi et al., 2024). The main advantages of CCIMS-nwA over other models for the eastern Canadian shelf (ECS) include: (a) vertical structures of currents and hydrography over coastal and shelf waters are better resolved by the the S-coordinate used in ROMS than the z-level ocean circulation models; (b) tidal forcing is included in the model external forcing; and (c) submodels of CCIMS-nwA can be easily relocated to any coastal waters of the ECS.

Three different nested-grid setups of CCIMS-nwA were made based on requirements and objectives of different research projects. Model results in three applications were examined, which demonstrate the feasibility and satisfactory skills of CCIMS-nwA in simulating 3D currents and hydrography over different coastal and shelf waters of the ECS. As part of the multi-agency research project entitled "reducing uncertainties on carbon cycling in Atlantic's North Western Seas" funded by the CFREF through the research program of "Transforming Climate Action", our future work includes coupling of CCIMS-nwA to the ocean surface wave model known as SWAN and examination of physical processes affecting the cycle and pathways of ocean carbon over the nwA using the coupled modelling system.

Acknowledgements

This study was supported by the Ocean Frontier Institute (Grant 38903), Natural Sciences and Engineering Research Council of Canada (Grant 217081), Marine Environmental Observation Prediction and Response Network (Grant 1-02-01-023.9), Department of Fisheries and Oceans Canada (Grant R35549) and Canadian Space Agency (Grant R36803). Numerical simulations were made on com-

putational resources maintained by the Digital Research Alliance of Canada. The authors sincerely thank Youyu Lu, Bruce Hatcher, Katja Fennel, and Eric Oliver for their suggestions and collaborations.

Conflicts of Interest

The authors declare no conflicts of interest regarding the publication of this paper.

References

Bourgault, D., & Koutitonsky, V. G. (1999). Real-Time Monitoring of the Freshwater Discharge at the Head of the St. Lawrence Estuary. *Atmosphere-Ocean, 37,* 203-220. https://doi.org/10.1080/07055900.1999.9649626

GEBCO Compilation Group (2019). *GEBCO 2019.* http://doi.org/10.5285/836f016a-33be-6ddc-e053-6c86abc0788e

Egbert, G. D., & Erofeeva, S. Y. (2002). Efficient Inverse Modeling of Barotropic Ocean Tides. *Journal of Atmospheric and Oceanic Technology, 19,* 183-204. https://doi.org/10.1175/1520-0426(2002)019<0183:eimobo>2.0.co;2

Haidvogel, D. B., Arango, H., Budgell, W. P., Cornuelle, B. D., Curchitser, E., Di Lorenzo, E. et al. (2008). Ocean Forecasting in Terrain-Following Coordinates: Formulation and Skill Assessment of the Regional Ocean Modeling System. *Journal of Computational Physics, 227,* 3595-3624. https://doi.org/10.1016/j.jcp.2007.06.016

Hunke, E. C. (2010). Thickness Sensitivities in the CICE Sea Ice Model. *Ocean Modelling, 34,* 137-149. https://doi.org/10.1016/j.ocemod.2010.05.004

Hunke, E., Lipscomb, W., Turner, A., Jeffery, N., & Elliott, S. (2015). *CICE: The Los Alamos Sea Ice Model Documentation and Software User's Manual Version 5.1.* LA-CC-06-012, Los Alamos National Laboratory.

Hunter, E. J., Fuchs, H. L., Wilkin, J. L., Gerbi, G. P., Chant, R. J., & Garwood, J. C. (2022). ROMSPath V1.0: Offline Particle Tracking for the Regional Ocean Modeling System (ROMS). *Geoscientific Model Development, 15,* 4297-4311. https://doi.org/10.5194/gmd-15-4297-2022

Jacob, R., Larson, J., & Ong, E. (2005). M × N Communication and Parallel Interpolation in Community Climate System Model Version 3 Using the Model Coupling Toolkit. *The International Journal of High Performance Computing Applications, 19,* 293-307. https://doi.org/10.1177/1094342005056116

Lellouche, J. M., Greiner, E., Bourdalle-Badie, R., Garric, G., Melet, A., Drevillon, M. et al. (2021). The Copernicus Global 1/12˚ Oceanic and Sea Ice GLORYS12 Reanalysis. *Frontiers in Earth Science, 9,* Article ID: 698876. https://doi.org/10.3389/feart.2021.698876

Marchesiello, P., McWilliams, J. C., & Shchepetkin, A. (2001). Open Boundary Conditions for Long-Term Integration of Regional Oceanic Models. *Ocean Modelling, 3,* 1-20. https://doi.org/10.1016/s1463-5003(00)00013-5

Mellor, G. L., & Yamada, T. (1982). Development of a Turbulence Closure Model for Geophysical Fluid Problems. *Reviews of Geophysics, 20,* 851-875. https://doi.org/10.1029/rg020i004p00851

Mesinger, F., DiMego, G., Kalnay, E., Mitchell, K., Shafran, P. C., Ebisuzaki, W. et al. (2006). North American Regional Reanalysis. *Bulletin of the American Meteorological Society, 87,* 343-360. https://doi.org/10.1175/bams-87-3-343

Ohashi, K., Laurent, A., Renkl, C., Sheng, J., Fennel, K., & Oliver, E. (2024). A Coupled

Circulation-Ice-Biogeochemistry Modelling System for the Northwest Atlantic Ocean: Development and Validation. *Geoscientific Model Development*.

Pawlowicz, R., Beardsley, B., & Lentz, S. (2002). Classical Tidal Harmonic Analysis Including Error Estimates in MATLAB Using T_TIDE. *Computers & Geosciences, 28,* 929-937. https://doi.org/10.1016/s0098-3004(02)00013-4

Pei, Q., Sheng, J., & Ohashi, K. (2022). Numerical Study of Effects of Winds and Tides on Monthly-Mean Circulation and Hydrography over the Southwestern Scotian Shelf. *Journal of Marine Science and Engineering, 10,* Article No. 1706. https://doi.org/10.3390/jmse10111706

Petrie, B., & Anderson, C. (1983). Circulation on the Newfoundland Continental Shelf. *Atmosphere-Ocean, 21,* 207-226. https://doi.org/10.1080/07055900.1983.9649165

Petrie, B., & Drinkwater, K. (1993). Temperature and Salinity Variability on the Scotian Shelf and in the Gulf of Maine 1945-1990. *Journal of Geophysical Research: Oceans, 98,* 20079-20089. https://doi.org/10.1029/93jc02191

Shchepetkin, A. F., & McWilliams, J. C. (2005). The Regional Oceanic Modeling System (ROMS): A Split-Explicit, Free-Surface, Topography-Following-Coordinate Oceanic Model. *Ocean Modelling, 9,* 347-404. https://doi.org/10.1016/j.ocemod.2004.08.002

Smagorinsky, J. (1963). General Circulation Experiments with the Primitive Equations: I. The Basic Experiment. *Monthly Weather Review, 91,* 99-164. https://doi.org/10.1175/1520-0493(1963)091<0099:gcewtp>2.3.co;2

Sui, Y., Sheng, J., Lu, Y., & Chen, S. (2024). Intense Lateral Intrusion of Offshore Sub-Surface Waters in Halifax Harbour. *Continental Shelf Research, 277,* Article ID: 105245. https://doi.org/10.1016/j.csr.2024.105245

Thompson, K. R., & Sheng, J. (1997). Subtidal Circulation on the Scotian Shelf: Assessing the Hindcast Skill of a Linear, Barotropic Model. *Journal of Geophysical Research: Oceans, 102,* 24987-25003. https://doi.org/10.1029/97jc00368

Thompson, K. R., Loucks, R. H., & Trites, R. W. (1988). Sea Surface Temperature Variability in the Shelf-Slope Region of the Northwest Atlantic. *Atmosphere-Ocean, 26,* 282-299. https://doi.org/10.1080/07055900.1988.9649304

Urrego-Blanco, J., & Sheng, J. (2012). Interannual Variability of the Circulation over the Eastern Canadian Shelf. *Atmosphere-Ocean, 50,* 277-300. https://doi.org/10.1080/07055900.2012.680430

Wang, Z., Li, D., Xue, H., Thomas, A. C., Zhang, Y. J., & Chai, F. (2022). Freshwater Transport in the Scotian Shelf and Its Impacts on the Gulf of Maine Salinity. *Journal of Geophysical Research: Oceans, 127,* e2021JC017663. https://doi.org/10.1029/2021jc017663

Yang, S., Sheng, J., Ohashi, K., Yang, B., Chen, S., & Xing, J. (2023). Non-Linear Interactions between Tides and Storm Surges during Extreme Weather Events over the Eastern Canadian Shelf. *Ocean Dynamics, 73,* 279-301. https://doi.org/10.1007/s10236-023-01556-w

Yashayaev, I., Peterson, I., & Wang, Z. (2022). *Meteorological, Sea Ice and Oceanographic Conditions in the Labrador Sea during 2020* (v + 62 p.). DFO Can. Sci. Advis. Sec. Res. Doc. 2022/039.